Available online at www.sciencedirect.com

jmr&t Journal of Materials Research and Technology

https://www.journals.elsevier.com/journal-of-materials-research-and-technology

Original Article

Impact of precipitates on the hydrogen embrittlement behavior of a V-alloyed medium-manganese austenitic stainless steel

Tarek Allam[a,b], *Xiaofei Guo*[a,*], *Marta Lipińska-Chwałek*[c,d], *Atef Hamada*[e,*], *Essam Ahmed*[b], *Wolfgang Bleck*[a]

[a] *Steel Institute (IEHK), RWTH Aachen University, D-52056 Aachen, Germany*
[b] *Department of Metallurgical and Materials Engineering, Suez University, 43528 Suez, Egypt*
[c] *Central Facility for Electron Microscopy, RWTH Aachen University, D-52074 Aachen, Germany*
[d] *Forschungszentrum Jülich GmbH, Ernst Ruska-Centre for Microscopy and Spectroscopy With Electrons (ER-C) and Peter Grünberg Institute, Microstructure Research (PGI-5), D-52425 Jülich, Germany*
[e] *Kerttu Saalsti Institute, University of Oulu, Pajatie 5, Nivala FI-85500, Finland*

ARTICLE INFO

Article history:
Received 1 August 2020
Accepted 24 September 2020
Available online 3 October 2020

Keywords:
Medium-manganese
Stainless steel
Precipitation
Thermal desorption analysis
Hydrogen embrittlement

ABSTRACT

This paper discusses the avoidance of hydrogen embrittlement (HE) in a medium manganese stainless steel X20CrNiMnVN18-5-10. We adopted a HE-mitigation strategy that relies on improving its intrinsic resistance to hydrogen by adjusting an ultrafine microstructure (~1.3 μm) containing a significant amount of nano-sized V- and Cr-based precipitates in the size range of 20 - ≥200 nm. The precipitation state was characterized using a high-resolution scanning transmission electron microscope. Slow strain rate tests at a strain rate of 10^{-6} s^{-1} were conducted on specimens with/without hydrogen pre-charging to evaluate the HE susceptibility. Thermal desorption analysis was applied to explore the hydrogen trapping behavior in cold-rolled, annealed and hydrogen pre-charged states. Hydrogen uptake and hydrogen desorption behaviors show a dependence on the size of precipitates. It is remarked that the large precipitates trap a larger amount of hydrogen and show a higher temperature desorption peak than the small precipitates do. The high-temperature hydrogen desorption peaks (>400 °C) indicate that the observed nano-sized precipitates provide irreversible trapping sites, where hydrogen uptake occurs. The investigated steel X20CrNiMnVN18-5-10 demonstrates an enhanced intrinsic resistance to HE in comparison to medium and high manganese as well as stainless steels. The findings suggest that microstructure engineering with sufficient number of hydrogen traps in an ultrafine-grained microstructure is an appropriate HE mitigation strategy that allows designing hydrogen-resistant advanced high strength steels.

* *Corresponding authors.*
E-mails: xiaofei.guo@iehk.rwth-aachen.de (X. Guo), atef.hamadasaleh@oulu.fi (A. Hamada).
https://doi.org/10.1016/j.jmrt.2020.09.085

1. Introduction

In recent years, high manganese steels (HMnS) with austenitic microstructure have attracted much research interests due to their excellent combination of strength and formability over other single phase or multi-phase structural steels [1,2]. Their extraordinary formability makes them promising candidates as cold deformable material in the design of light-weight structural applications. Such exceptional strength and formability properties of HMnS are attained through transformation induced plasticity (i.e. martensitic transformations) and/or twinning induced plasticity (TWIP) effects, which can be controlled by the intrinsic factor of stacking fault energy (SFE) [1,3]. Although the formation of martensite and twins enables achieving a high work hardening rate for HMnS, it can lead to local inhomogeneity [4,5] that significantly increases their susceptibility to hydrogen embrittlement (HE) [3,5]. Consequently, this limits the ultimate utilization of their excellent formability in service environment.

Several studies have been dedicated to improve the relatively poor wet corrosion resistance of HMnS resulting from the high dissolution rate of Mn [6] by utilizing various additions of alloying elements such as Al and Cr [7–10]. Nitrogen was demonstrated as an effective element in raising the pitting corrosion resistance [11,12]. Furthermore, it significantly stabilizes austenite phase allowing the tuning of alloy design of HMnS by partial substitution of Mn and C in HMnS, and similarly in alloy design of stainless steel by reducing Ni and C contents [12–18]. Consequently, the development of Fe-Cr-Mn-N TWIP stainless steels have recently received a great attention, since they have the potential to maintain the exceptional mechanical properties of HMnS along with enhanced corrosion resistance of stainless steels [14]. The addition of Mn and N stabilizes the austenite phase, however, adding Cr to the system stabilizes austenite phase at lower N contents, and stabilizes h.c.p. phase at higher N content. This was explained by the thermodynamic description of h.c.p. phase as Cr_2N nitride [15].

Regarding the HE in HMnS, several investigations have been conducted to understand its behavior with respect to alloy design, stress states, and microstructural features [3–5,19,20]. The high solubility of diffusive hydrogen in the austenite microstructure and hydrogen enrichment at stress concentrated regions are found to be the major factors that lead to poor HE resistance. These stress concentrated regions are induced by the twin-twin or twin-grain boundary intersections [20,21], segregations or unfavorable inclusions at grain boundaries [22]. Among the suggested methodologies to alleviate HE in HMnS are addition of substitutional alloying elements such as Al and Cu, grain refinement, or introducing hydrogen traps. Al and Cu, were found to be effective in raising the SFE and in suppressing the formation of deformation twins [2,20,23–25]. Moreover, the improved corrosion resistance due to the passivation effect by Al and Cu limits the hydrogen ingression and enhances the HE resistance [7,19]. The suppression of deformation twins and the resulting stress localization by grain refinement has been proven to be effective in enhancing the HE behavior [26,27]. The grain refinement in HMnS was demonstrated by utilizing various micro-alloying elements such as V, Nb and Ti to control the grain size through precipitation-induced grain boundary pinning effect [1]. In addition to the indirect role of precipitates in improving HE behavior (due to grain refinement), their direct role as hydrogen traps is still a matter of research [28–30]. The role of k-carbides as hydrogen trapping sites in HMnS was investigated [31]. Moreover, the Cr-based and V-based precipitates were reported to act as traps for mobile hydrogen and consequently can reduced the susceptibility to HE in high strength ferritic and martensitic steels [32–36]. It was found that the hydrogen trap ability depends on type and coherency of the precipitates to the matrix as well as their surface area [34,36].

In spite of the developments to improve the material-related issues of HMnS such as low yield strength and poor corrosion and HE behaviors, the technological challenges related to their processing limit their applications. Recently, there has been a growing academic and industrial interest in medium manganese steels (MMnS) due to their excellent mechanical properties and reduced production costs compared to HMnS [37–40]. Furthermore, medium manganese stainless steels (MMnSS) with austenitic microstructures have been developed utilizing the various alloy design considerations namely, grain refinement, precipitation hardening, TWIP effect, and pitting and corrosion resistance. Hamada et al. [41] designed a 8Mn-16Cr-3Ni-Mo-V-N austenitic steel and demonstrated its excellent yield, tensile strengths and elongation of 700 MPa, 1100 MPa and 30 % respectively. In a further study [42], they investigated the effect of low and high Si content on the hot formability of X20CrNiMn(Si)VN18-5-10 steels. Most recently, Allam et al. [43] demonstrated the enhanced mechanical and corrosion properties of X20CrNiMnVN18-5-10 steel by adjusting an ultrafine grain microstructure with a significant amount of nano-precipitates. However, the impact of the nano-precipitates on the HE behavior of this newly developed X20CrNiMnVN18-5-10 MMnSS grade has not been reported yet. Hence, the current study introduces a comprehensive characterization of the hydrogen trapping behavior in the presence of a significant amount of nano-precipitates using the thermal desorption spectrometry (TDS). The HE susceptibility of the X20CrNiMnVN18-5-10 steel was investigated by performing slow strain rate tests (SSRT) under different hydrogen charging conditions and was compared with those of conventional TWIP and stainless reference steels. The susceptibility to HE and the hydrogen trapping behavior of the X20CrNiMnVN18-5-10 MMnSS were further discussed with respect to the nanoprecipitation state characterized using high-resolution scanning transmission electron microscope (STEM).

2. Material and methods

2.1. *Materials*

The investigated steel X20CrNiMnVN18-5-10 was produced through induction melting and ingot casting processes. A 50 Kg melt was casted in ingots of $170 \times 160 \times 60\,mm^3$. The ingots were homogenized at 1200 °C for 4 h and hot-forged down to 12 mm thick slabs, which were further

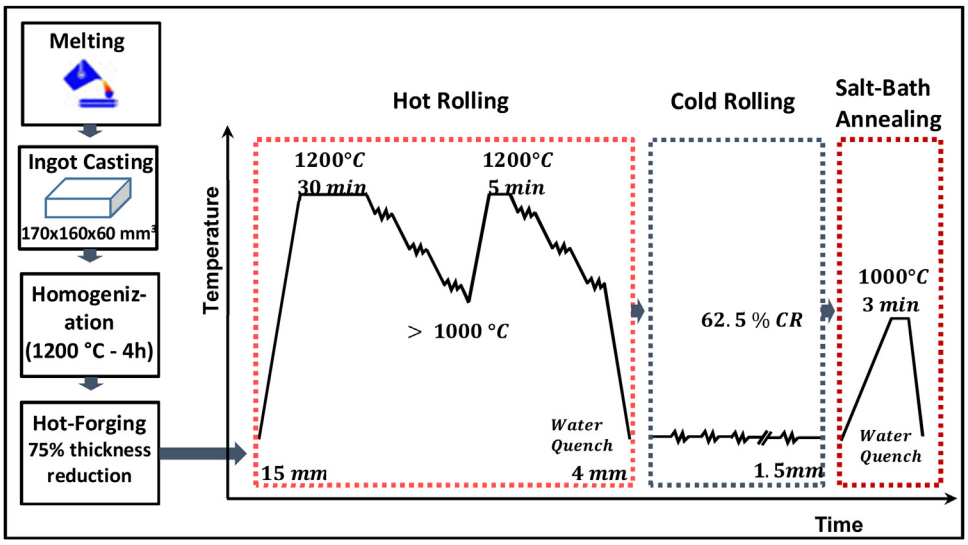

Fig. 1 – Laboratory processing route of the investigated steel X20CrNiMnVN18-5-10.

Table 1 – Chemical composition in wt.% of the X20CrNiMnVN18-5-10 steel.

Materials	C	Si	Mn	P	S	Cr	Ni	V	N
X20CrNiMnVN18-5-10	0.17	0.43	10.4	0.014	0.009	17.7	4.7	0.9	0.267

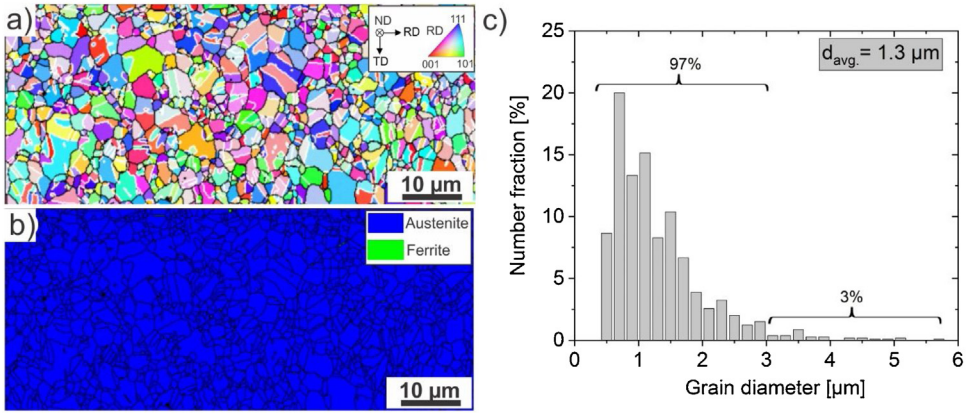

Fig. 2 – Electron backscatter diffraction (EBSD) analysis of the X20CrNiMnVN18-5-10 steel after recrystallization annealing at 1000 °C for 3 min. (a) Inverse pole figure in the rolling direction (RD). (b) Phase fraction map. c) Grain size distribution profile. Reproduced from [43].

hot and cold rolled to a final thickness of 1.5 mm as illustrated in Fig. 1. The chemical composition was measured by optical emission spectrometer and is listed in Table 1.

The required specimens were manufactured from the cold-rolled sheets and subjected to a recrystallization annealing heat treatment at 1000 °C for 3 min. The applied heat treatment was adopted from a previous study [43] to adjust an ultrafine recrystallized austenitic microstructure with a significant amount of precipitates. The initial as-annealed microstructure and the corresponding grain size distribution are depicted in Fig. 2, which shows a fully recrystallized austenite grains with a random orientation relationship and an average grain size of 1.3 µm.

2.2. *Characterization of size and chemical composition of the different precipitates*

Carbon extraction replica method was applied to prepare the electron transparent specimens required for characterizing the state of precipitates in the as-annealed condition. The bright field images of the extracted precipitates were captured using a FEI Tecnai F20 transmission electron microscope (TEM) operated at 200 kV [44]. Furthermore, a detailed analysis of size distribution and chemical composition of the different precipitates was performed through high angle annular dark field (HAADF) imaging and energy dispersive X-ray (EDX) spectral mapping, respectively, using a FEI Titan G2 80–200 high-resolution Cs probe corrected scan-

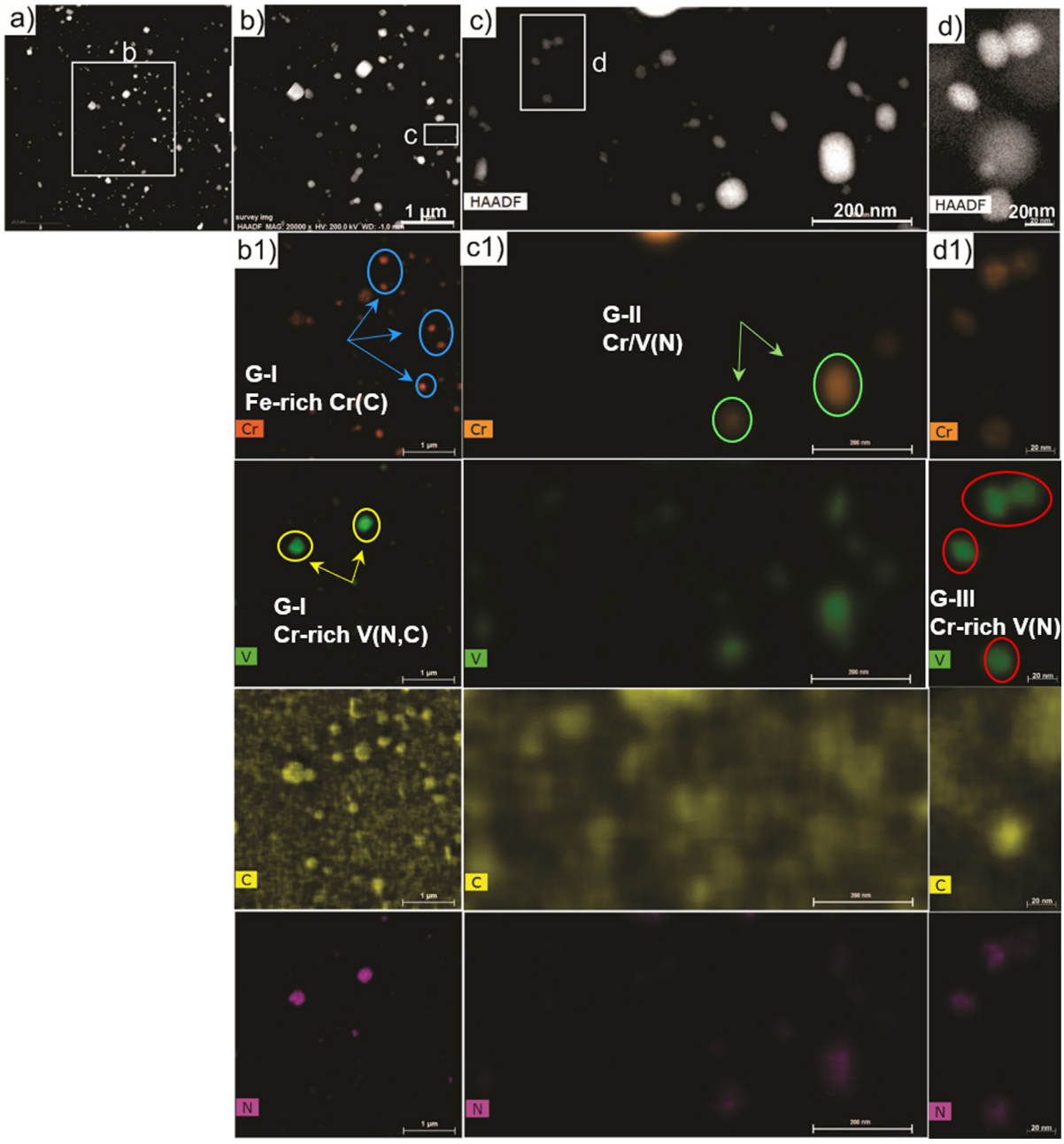

Fig. 3 – STEM HAADF images and the corresponding EDX-spectral maps of the carbide and nitro-carbide precipitates extracted from the bulk annealed X20CrNiMnVN18-5-10 steel on the carbon-supported TEM replicas. (a) a representative HAADF micrograph of the all precipitates. (b), (c) and (d) represent HAADF micrographs of the white rectangles in (a), (b) and (c) at high magnification, respectively. (b1), (c1) and (d1) are the EDX-spectral maps of the corresponding HAADF micrographs. The blue circles show the large Fe-rich Cr(C) precipitates ~200 nm. The yellow circles represent the largest Cr-rich V(N,C) precipitates >200 nm. Light-green circles refer to Cr-rich V(N) and V-rich Cr(N) with an average size of ~100 nm. The red circles show the smallest Cr-rich V(N) precipitates of ~20 nm.

ning transmission electron microscope (STEM) operated at 200 kV [45]. With the help of ESPRIT software of Bruker Company the acquired EDX spectral maps were analyzed, while the size of the precipitates was measured using Image J® software on the HAADF STEM micrographs of an arbitrarily selected areas of extraction replicas (each of 6 μm × 6 μm in size).

2.3. *Galvano-static hydrogen charging*

Diffusive hydrogen was introduced into the specimens by electrochemical charging in 0.05 M H_2SO_4 at a constant current density of 5 mA/cm^2 and a temperature of 40 °C for 24 h. 1.4 g/l CH_4N_2S was added to the charging solution to suppress the re-combination of H atom into H_2 and to promote the

Table 2 – The size and chemical composition analysis of the identified precipitates using EDX spectral maps in STEM.

Precipitation period	Size group	Precipitate type		Relative contents of alloying elements in at. % without C			
	Avg. diam. (nm)	Calculated ThermoCalc [43]	Experimental STEM/EDX maps	V	Cr	Fe	N
During casting and rolling	(G–I) ≥200	MN	Cr-rich V(N,C)	50–55	10	<0.5	34–40
		M23C6	Fe-rich Cr(C)	3–6	70–75	20–24	0
During annealing	(G–II) ~100	M2N	V-rich Cr(N)	20–30	37–55	1–4	10–30
		MN	Cr-rich V(N)	43–46	8–9	<0.5	45–48
	(G–III) ~20	MN	Cr-rich V(N)	40–60	6–14	«0.5	40–50

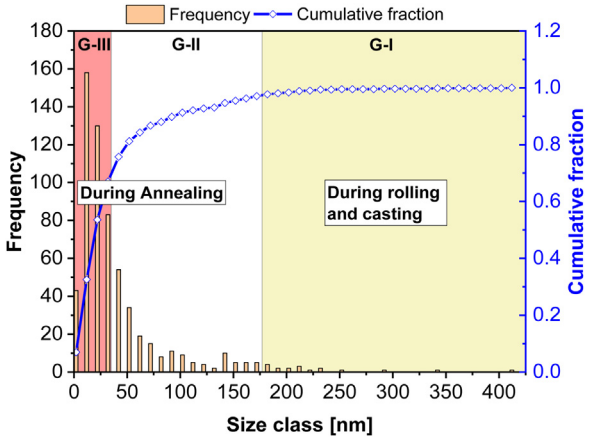

Fig. 4 – Size distribution analysis of the observed precipitates showing the frequency of different size groups and corresponding cumulative fraction.

hydrogen ingression. Before charging, the specimen surfaces were mechanically grinded up to grit 1200 and subsequently polished using 6 μm polishing clothes. After charging, the specimens were ultrasonic cleaned and stored in liquid N_2 for further hydrogen measurement or mechanical testing.

2.4. *Slow strain rate tests*

The susceptibility to hydrogen embrittlement was investigated by performing slow strain rate tests (SSRT). Annealed specimens with and without pre-charging are tested in SSRT. The pre-charged specimens were tested in a cleaned and a dried state immediately after their removal out of the liquid N_2 storage. A constant extension machine (Company Fritz) was used to carry out the SSRT at a strain rate of $10^{-6}\,s^{-1}$ until fracture. The applied specimens (3 for each conditions) were manufactured in the rolling direction with a gauge length of 25 mm, width of 5 mm and a thickness of 1.5 mm.

2.5. *Hydrogen measurements*

The thermal desorption spectrometry (TDS) was utilized to study the hydrogen trapping behavior using TDS-System Bruker Galileo 8. The TDS measurements were conducted on specimens in different conditions, namely, cold-rolled, annealed and pre-charged (in annealed condition) states. The corresponding hydrogen desorption rate curve for each state was recorded during heating at a constant heating rate of 20 °C/min from room temperature to 800 °C for the pre-charged state and to 900 °C for the cold-rolled and annealed states. The desorption peaks were further fitted using Origin® according to the Lorentzian peak function to analyze and fit the different diffusive/trapping hydrogen desorption peaks.

2.6. *Characterization of fracture surfaces*

The influence of hydrogen pre-charging on the fracture characteristics was investigated by examining the fracture surfaces of the SSRT specimens using a Zeiss Sigma field emission scanning electron microscopy (FE-SEM) at an operating voltage of 15 kV.

3. Results

3.1. *Characterization of the precipitation state*

Understanding the hydrogen trapping behavior in the X20CrNiMnVN18-5-10 steel requires a detailed identification of the existing precipitates. The TEM-observations demonstrated the presence of various precipitates with different sizes and chemical compositions. In general, they can be classified into three distinguished groups based on the size: (G-I) largest precipitates with an average diameter of ≥200 nm, (G-I I) relatively large precipitates with an average diameter of about 100 nm and (G-I II) that represents the smallest precipitates with an average diameter of 20 nm. In Fig. 3, the STEM HAADF micrographs and the corresponding EDX spectral maps of the precipitates extracted from the bulk material on carbon-supported TEM replicas. Fig. 3a shows a representative HAADF micrograph of the replica area where the three precipitate groups were observed. The regions inside the white rectangles in Fig. 3a, b and c are represented in higher magnifications in Fig. 3b, c and d, respectively. The columns of images in Fig. 3b1, c1 and d1 depict the corresponding EDX maps of the above HAADF micrographs in Fig. 3b, c and d, respectively.

The chemical compositions of the precipitates, identified with STEM/EDX analysis of the extraction replicas, are summarized in Table 2, which additionally provides the corresponding size group, formation stage and the thermodynamically calculated types of precipitates. The given chemical compositions represent the relative ratios of the atomic content for the respective elements without considering carbon. The carbon content was omitted during the analysis, since the signal from the background with carbon replica of an irregular thickness influences the accuracy of the carbon content.

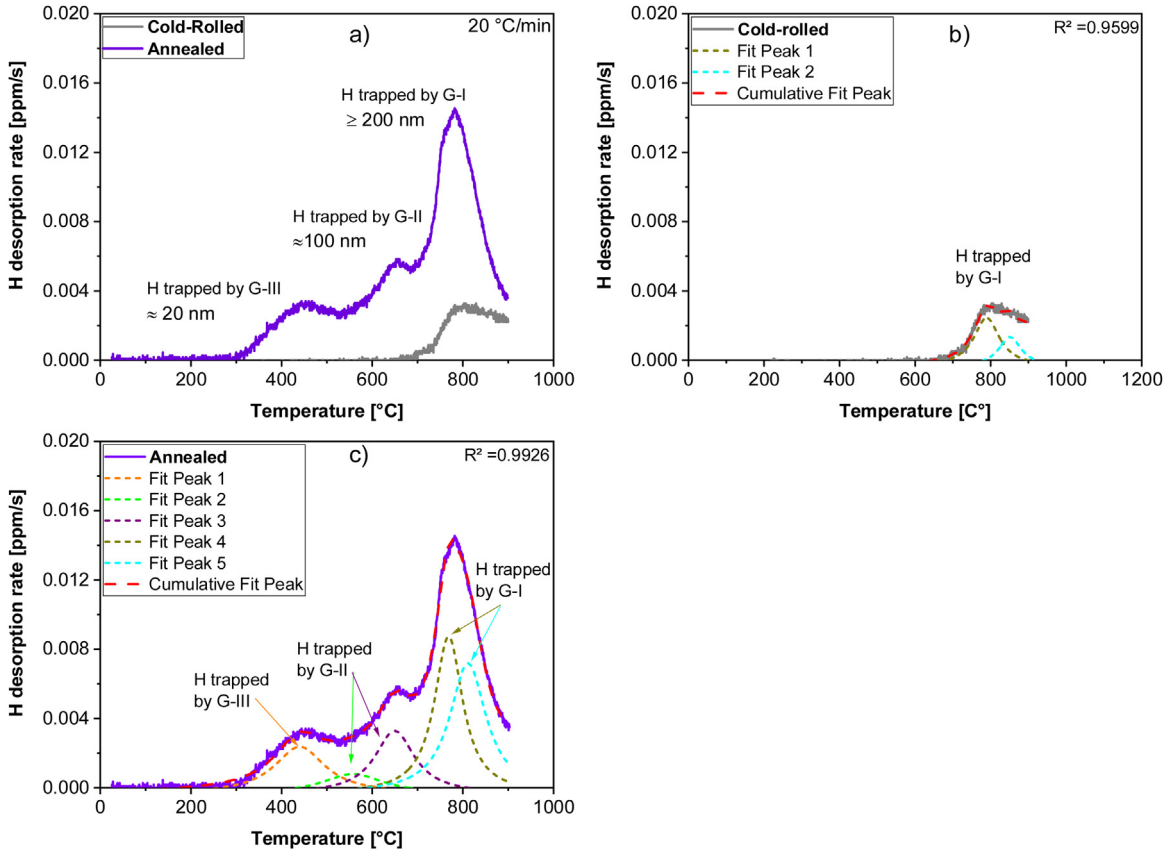

Fig. 5 – (a) Thermal desorption spectroscopy (TDS) curves without hydrogen charging for the cold-rolled and annealed states. (b) and (c) corresponding peak fitting analysis according to Lorentzian peak function for the cold-rolled and annealed states, respectively.

The observations from STEM/EDX maps and the corresponding chemical analysis confirmed the formation of MN-type precipitates in the form of Cr-rich V(N,C) with a large average size of >200 nm (yellow circles below Fig. 2b1) and Cr-rich V(N) with a very small average size ~20 nm (red circles in Fig. 2d1). The Fe-rich Cr(C) that corresponds to M23C6-type was found only with a large average size of ~ 200 nm (blue circles in Figure 2b1). Furthermore, the thermodynamically unstable M2N-type (at 1000 °C) was observed in the form of V-rich Cr(N) besides, the Cr-rich Vr(N) with a relatively large average size of 100 nm (light-green circles in Fig. 2c1). The size distribution analysis of the observed precipitates is represented in Fig. 4. It is clear that more than 50% of all precipitates is ≤ 20 nm in size, whereas the large precipitates with sizes of ≥200 nm resemble a small relative fraction of around 2% of all precipitates.

3.2. *Hydrogen trapping behavior*

3.2.1. *Thermal desorption spectroscopy without hydrogen pre-charging*

Fig. 5a shows the TDS curves (hydrogen desorption rate against temperature) in the cold-rolled and annealed states. These curves were obtained for corresponding specimens without hydrogen pre-charging. For the cold-rolled state, the TDS curve starts showing a visible increase in the hydrogen desorption rate at temperatures higher than 700 °C represented in a single broad peak near 800 °C. However, the TDS curve of the annealed state indicates three distinguished broad peaks over a wide temperature range, which become prominent at temperatures above 400 °C. In general, for the two states without hydrogen pre-charging, the visible desorption peaks account for the irreversibly trapped hydrogen at various groups of precipitates of different sizes.

To explore the hydrogen trapping behavior and to identify the different hydrogen irreversible traps in X20CrNiMnVN18-5-10 steel, peak fit analysis was further performed on the obtained TDS curves. The fitted TDS curves for both cold-rolled and annealed states are shown in Fig. 5b and c, respectively. Two separate peaks appear for the cold-rolled state, which are arising out of the hydrogen desorption at 790 and 851 °C and accounting for a total hydrogen content of approximately 1.68 ppm trapped by G-I of the precipitates. The TDS curves of the annealed state is deconvoluted in five peaks as depicted in Fig. 5c. All of the hydrogen desorption peaks are fitted in the high temperature range (400–800 °C), and they correspond to a total hydrogen content of approximately 11.13 ppm trapped by all groups of the precipitates. The trapped hydrogen by the largest size precipitates (G-I ≥200 that formed during production) is desorbed in the high temperature range at 769 °C (peak 4) and 811 °C (peak 5) similar to that is observed in the cold-rolled state. Interestingly, the precipitates formed dur-

Table 3 – A summary of the hydrogen contents, which are calculated from fitted peaks of the obtained thermal desorption spectroscopy curves for the cold-rolled, annealed and pre-charged states.

State	Diffusive H [ppm]		Trapped H [ppm] desorbed at different T [°C]												Total diffusive H [ppm]	Total H [ppm]
			Reversible		Irreversible											
			Lattice defects		G–III ~ 20 nm		G–II ~ 100 nm				G–I ≥200 nm					
	H	T	H	T	H	T	H	T	H	T	H	T	H	T		
Cold-rolled	–	–	–	–	–	–	–	–	–	–	1.10	790	0.58	851	–	1.68
Annealed	–	–	–	–	1.74	440	0.88	558	1.81	650	3.24	769	3.46	811	–	11.13
Pre-charged*	11.5	260	0.83	371	1.94	443	6.99	609	0.38	770	–	–	–	–	11.50	21.64

* The hydrogen desorption rate curve was recorded from room temperature up to 800 °C.

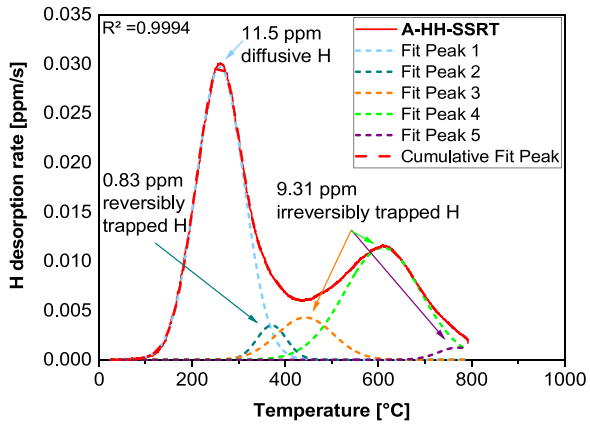

Fig. 6 – Thermal desorption spectroscopy curves of the pre-charged state after testing in SSRT with peak fitting analysis according to Lorentzian peak function.

ing annealing and represented by relatively large precipitates (G-I I ~ 100 nm) and small precipitates (G-I II ~ 20 nm) are releasing hydrogen at relatively lower temperatures. It is to be additionally remarked that the amount of desorbed hydrogen from G-I precipitates in the annealed state (~6.7 ppm) is larger than its counterpart in the cold-rolled state. The average hydrogen contents associated with the fitted peaks for all the cold-rolled, annealed and pre-charged states as well are summarized in Table 3.

3.2.2. *Thermal desorption spectroscopy with hydrogen pre-charging*

The hydrogen desorption behavior for the pre-charged state was analyzed based on the thermal desorption spectra recorded during heating at a constant heating rate of 20 °C/min from room temperature up to 800 °C. The resultant TDS curve and the corresponding peak fit analysis are superimposed and represented in Fig. 6. In contrary to the uncharged states represented in the previous section, the pre-charged state shows a prominently large peak at relatively low temperature of 260 °C, which is regarded as a diffusive hydrogen peak.

The superimposed peak fit analysis indicates the presence of 5 desorption peaks until 800 °C. The prominent peak at 260 °C accounts for a total diffusive hydrogen of 11.50 ppm. A further hydrogen desorption peak is identified within the relatively low temperature range at 371 °C, which represents the reversibly trapped hydrogen with a hydrogen content of 0.83 ppm. The diffusive and reversibly trapped hydrogen can be desorbed at low temperature intervals (of 260 and 371 °C, respectively), if located at the lattice defects of low hydrogen desorption energies, such as interstitials, dislocations and grain boundaries. On the contrary, the irreversibly trapped hydrogen shows its desorption peaks at higher temperature intervals of 443, 609 and 770 °C, as this irreversible hydrogen is captured at the sites of relatively high desorption energies, such as the different size-groups of precipitates found in the investigated material. The third peak, observed at 443 °C, is attributable to the hydrogen desorbed from the smallest size-group of precipitates G-I II (~20 nm) of around 1.94 ppm. Up to 800 °C, additional two peaks are fitted at 609 and 770 °C and they supposedly account for the hydrogen released from the relatively large-size precipitates G-I I (~ 100 nm) of 7.37 ppm. Accordingly, the total irreversibly trapped hydrogen by G-I I and G-I II of precipitates in the pre-charged state was calculated to be 9.31 ppm, while the total hydrogen content desorbed during heating up to 800 °C is analyzed to be 21.64 ppm. Based on the analysis of TDS curve and the hydrogen contents listed in Table 3, It is readily discernible that the desorbed hydrogen from G-I II precipitates in pre-charged state (1.94 ppm) is not significantly higher than that desorbed from the same precipitates in the annealed state (1.74 ppm). Whereas, the hydrogen desorbed from G-I I precipitates in the pre-charged state (7.37 ppm) is considerably higher than that in the annealed state (2.69 ppm).

3.3. *Susceptibility to hydrogen embrittlement*

The susceptibility to hydrogen embrittlement of X20CrNiMnVN18-5-10 steel was evaluated by means of SSRT applied at a strain rate of 10^{-6} s^{-1}. Fig. 7a shows the recorded stress-strain curves for the annealed and pre-charged states. The susceptibility to hydrogen embrittlement

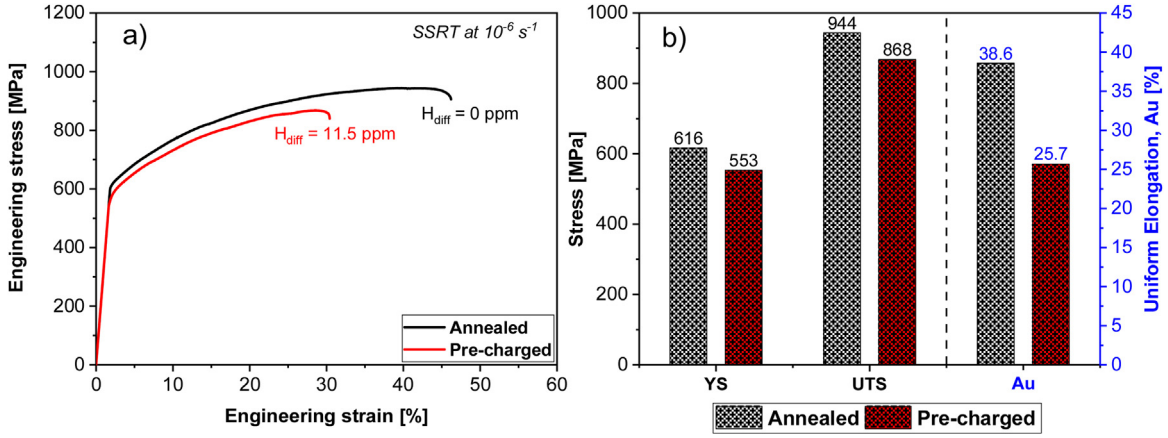

Fig. 7 – Susceptibility of X20CrNiMnVN18-5-10 steel to hydrogen embrittlement evaluated by slow strain rate tests (SSRT) in annealed and pre-charged states. (a) stress-strain curves recorded at strain rate of 10^{-6} s^{-1}. (b) bar chart for the corresponding mechanical strength and ductility values.

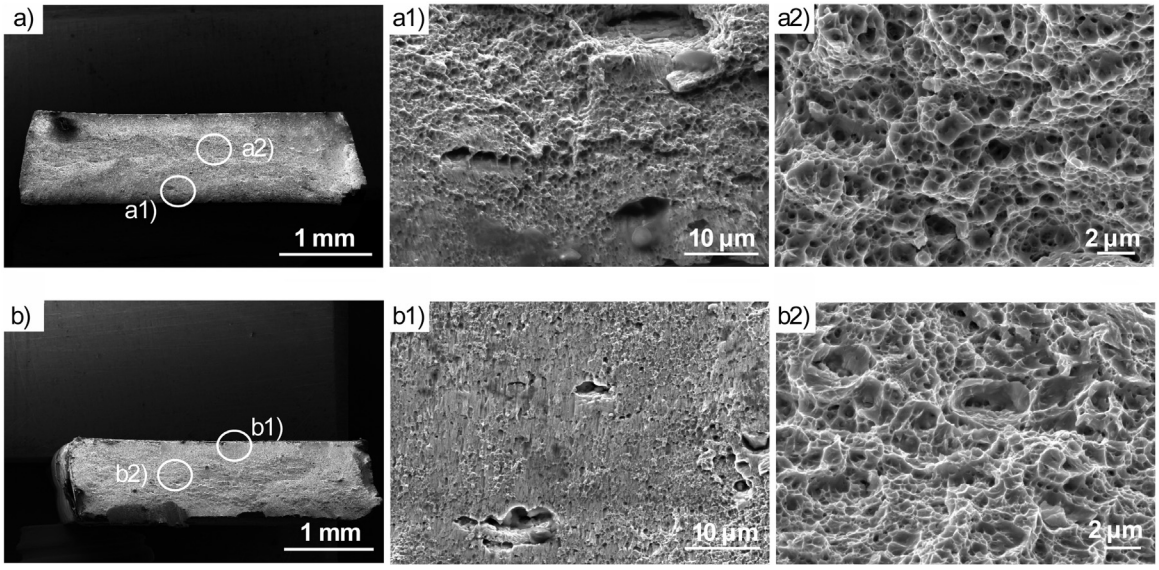

Fig. 8 – FE-SEM micrographs of the fracture surfaces for annealed and pre-charged states. (a-a2) and (b-b2) different regions of fractures surface for the annealed and hydrogen pre-charged states, respectively.

represented by the changes in yield strength (YS), ultimate tensile strength (UTS) and uniform elongation (Au) is shown as bar chart in Fig. 7b. A relatively remarkable reduction in Au value can be observed for the pre-charged state containing a significant amount of diffusive hydrogen (11.5 ppm), as it decreases from 38.6% in the annealed state to 25.7 %. With respect to strength level, the annealed state exhibits a YS and an ultimate UTS of 616 and 944 MPa, respectively. In spite of the large amount of diffusive hydrogen, the pre-charged state still exhibits satisfactory mechanical strength values compared with the annealed state, as the YS decreases to 553 MPa, whereas the UTS reveals 868 MPa.

3.4. *Fracture surfaces*

Investigating the fracture surfaces after conducting SSRT allows to reveal the influence of hydrogen pre-charging on the fracture characteristics. Fig. 8 shows FE-SEM micrographs of fracture surfaces for the annealed as well as the hydrogen pre-charged states. In Fig. 8a, an overview of the fracture surface for the annealed state is represented. More detailed views of the near surface and center regions are depicted in Fig. 8a1 and a2, respectively. Both regions are featured with very fine dimples which indicate a ductile fracture mode. The general overview of the fracture surface for the hydrogen pre-charged state is shown in Fig. 8b. Near the surface, the hydrogen pre-charged state shows a sheared layer, which indicates the prevailing of a trans-granular brittle fracture mode near the surface. The sheared layer is relatively deep in the hydrogen pre-charged state as can be seen in Fig. 8b1. However, the central fracture region depicted in Fig. 8b2 display the characteristic dimples of ductile fracture mode similar to that observed for the annealed state without hydrogen pre-charging.

4. Discussion

4.1. *Precipitates and hydrogen trapping behavior*

The MN-type and M23C6-type are the equilibrium precipitates at 1000 °C (annealing temperature), however, the precipitation kinetics calculations indicated the suppression of M23C6-type and the promotion of M2N-type at the same temperature within three minutes (annealing time), as indicated in Fig. 9. Interestingly, the STEM/EDX maps and the compiled chemical analysis demonstrate the presence of the three precipitate-types with different sizes in the recrystallized-annealed state. It seems that the applied hot-rolling schedule, which involved a relatively longer time than applied for precipitation kinetics calculations, promoted the formation of M23C6-type precipitates. Combining the thermodynamic and kinetics calculations with the STEM/EDX observations and analysis, it turns out that the formation of Cr-rich V(N,C) and Fe-rich Cr(C) precipitates (G-I) with a particle size of ≥200 nm and small relative fractions of around 0.02 is inevitable during production due to the considerable amounts of Cr, V and N. While, the smallest Cr-rich V(N) precipitates (G-I II) with particle size of ~20 nm and the relatively large Cr/V-rich V(N) precipitates (G-I I) with particle size of ~ 100 nm are induced by recrystallization annealing. Owing to the presence of this considerable amount of various precipitates with around 80% smaller in size than 50 nm a superior strength-ductility balance (yield strength of 600 MPa, tensile strength of 975 MPa and total elongation of 45%) as well as a high initial work hardening rate (~ 3.4 GPa) was established [43].

The role of precipitates in X20CrNiMnVN18-5-10 steel is not limited to adjustment of mechanical properties, rather, it extends to enhancement of its hydrogen trapping behavior, which is introspected as follows. In Fig. 5, the TDS analysis of the annealed state without hydrogen pre-charging reflects dif-

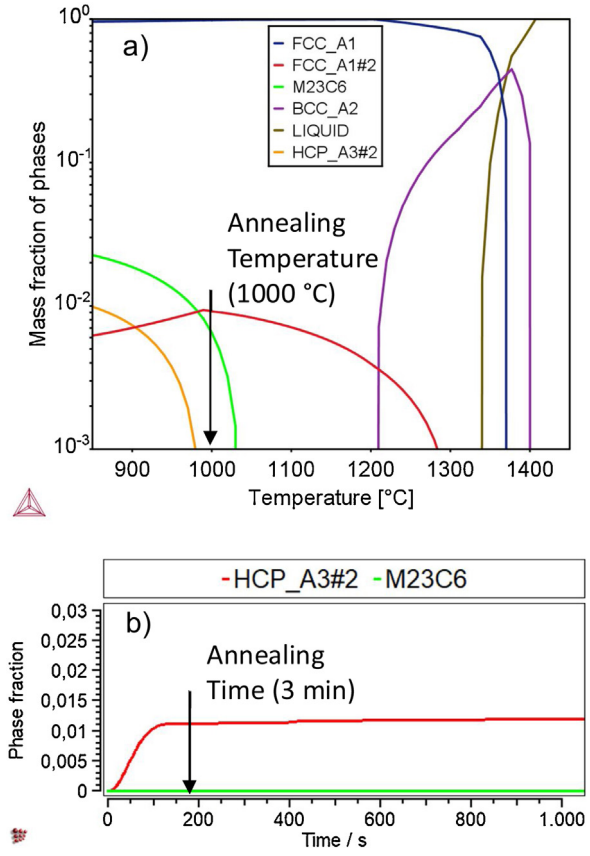

Fig. 9 – Thermodynamic calculation and precipitation kinetics. (a) ThemoCalc calculations (TCFE9) representing the fraction of equilibrium phases vs. temperature indicating that the austenite (FCC_A1) is in equilibrium with M23C6 and MN (FCC_A1#2) type of precipitates at the applied annealing temperature of 1000 °C. (b) MatCalc calculations (version 6.02) showing the precipitation kinetics and revealing the formation of M2N type of precipitate (HCP_A3#2). BCC_A2 stands for ferrite.

ferent desorption behaviors for the observed three size-groups of precipitates, which can be easily decipherable in terms of heights of the three broad peaks and their corresponding desorption temperatures. These behaviors demonstrate different tapping abilities (amount of desorbed hydrogen) and energies (related to desorption temperature), which is supposedly attributable to the differences in their type and size groups. A further observation from the TDS curve is that the hydrogen desorption from all precipitates happens within the high temperature range (>400 °C), indicating high energy barriers of strong [46] and irreversible [47] trapping sites. Moreover, the sequence of desorption peaks with respect to temperature suggests that the larger the precipitate size, the higher the activation energy and the amount of trapped hydrogen, as reported by Lee et al. [48], who related the increase in trapping activation energy of hydrogen with increasing particle size. Furthermore, Koyama et al. [49] demonstrated that the differences in coherency due to the elastic strain field induced by misfit dislocations around the precipitates can be a reason for the variation in activation energies and the corresponding desorption temperatures. This is in line with our results obtained for the cold-rolled state material, that includes only the largest size of precipitates, which desorb the trapped hydrogen at the highest temperatures. However, determination of the activation energy for each individual precipitate still requires further TDS analysis at different heating rates to develop Kissinger plots [50].

Technically, the short annealing heat treatment cycle is considered to promote fine V-based precipitates with high degree of coherency, since long time heat treatment at high temperature can promote coarsening of the precipitates and eventually lead to a loss of coherency and a subsequent degradation in mechanical properties [51]. The G-I of precipitates that formed during production steps are relatively large (≥200 nm) and most probably incoherent with a considerable number of misfit dislocations to accommodate the resulting elastic strain field around the precipitates. However, those formed during the short annealing heat treatment are assumed according to their sizes to be coherent (G-I II) or semi-coherent (G-I I) with a smaller number of misfit dislocations. Accordingly, the observed Fe-rich Cr(C) and Cr-rich V(N,C) precipitates of large sizes are considered deep irreversible traps for hydrogen that can be desorbed only at high temperatures (770–800 °C). Although the high fraction of the Cr-rich V(N) precipitates, their small average sizes (~20 nm) and assumed coherent character account for the observed lower hydrogen desorption temperatures (440–485 °C) and the relatively weaker trap ability. The Cr/V(N) precipitates exhibit a moderate hydrogen trapping ability as their sizes are intermediate between the other two types. It seems that size-dependent coherency of different observed precipitates is more significant than their relative fractions with respect to desorption energy and trapping ability. A quantitative analysis of hydrogen trapping and kinetics of Fe-Ti-C alloys showed that the coherent TiC hydrogen traps are not as effective as incoherent ones, and the large TiC precipitates are characterized by a long hydrogen de-trapping time [52,53]. It is still hard to conclude whether the hydrogen is likely to be residing in the vicinity or inside the trapping precipitates without calculating the energy barrier between the matrix and the precipitates interface [54]. The first-principles calculations using density function theory of hydrogen interaction with TiC precipitates showed the possibility of trapping hydrogen at different types of interfaces between the TiC particle and matrix, at misfit dislocations and also at the carbon vacancies inside TiC [55].

4.2. *Hydrogen uptake*

Hydrogen uptake in steel can occur during its production (metallurgical hydrogen), its manufacturing (hydrogen ingression, especially during annealing and galvanizing) and in service (environmental hydrogen). In spite of the various measures that can be taken to limit the quantity of metallurgical hydrogen during steel making [56], hydrogen ingression is unavoidable during processing, manufacturing (blanking, cutting, forming and joining) [57] and in service from other external environmental sources [54]. In the current study, the production processes till cold-rolling resulted in hydrogen uptake with a total hydrogen of 1.68 ppm, which increased to 11.13 ppm after annealing and subsequent water quench as

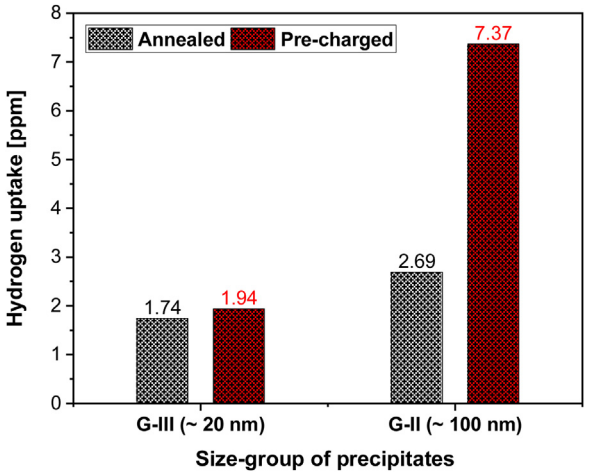

Fig. 10 – Comparison of the hydrogen uptake induced by pre-charging at both of G-II and G-III types of precipitates.

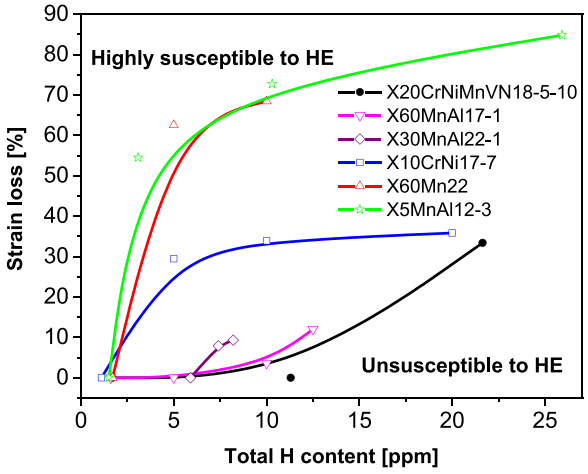

Fig. 11 – Strain loss at different total hydrogen contents of the investigated X20CrNiMnVN18-5-10 steel compared with other HMnS (X60Mn22, X60MnAl17-1 and X30MnAl22-1 [60]), MMnS (X5MnAl12-3 [63]) and stainless steel (X10CrNi17-7 [65,66]).

identified by TDS analysis in Fig. 5 and Table 3. Such increase in the hydrogen content in annealed state is attributable to the hydrogen ingression at high temperature from the salt bath at the significant number of precipitates formed during annealing, as well as during the subsequent water quench. This adsorbed level of hydrogen is considerably high and even much higher than that bearings for off-shore can accumulate over their lifetime (~3 ppm) [54]. On the one hand, the further occurrence of two broad peaks due to annealing (in addition to the one observed in the cold-rolled state) emphasizes the role of formed precipitates in the increase of hydrogen uptake and hydrogen trapping ability, as it is affirmed from the increase in hydrogen content. On the other hand, the conjecture that the hydrogen ingress during annealing is irreversibly trapped at the formed significant number density of V- and Cr-based precipitates is confirmed by the observed high temperature desorption peaks (>400 °C).

The TDS curve and hydrogen analysis of the pre-charged state reveal that the microstructure is still able to trap more hydrogen up to 9.31 ppm in the irreversible trapping sites (at G-I I and G-I II precipitates up to 800 °C), besides 0.83 ppm in the reversible sites. The diffusive and reversibly trapped hydrogen is assumed to be accommodated at the normal interstitial lattice sites, at the dislocations as well as at the large grain boundary areas owing to the ultrafine grained microstructure with an average grain size of 1.3 μm. It is worth noting that the hydrogen uptake induced by pre-charging at G-I I precipitates (from 2.69 to 7.37 ppm) is significantly higher than that occurs at G-I II precipitates (1.74–1.94 ppm) as indicated in Fig. 10, attributable to the size effect as it is already discussed in the previous section.

4.3. *Hydrogen embrittlement behavior*

The accumulated knowledge of HE mitigation emphasizes the prime importance of controlling the amount of diffusible hydrogen within the microstructure, as the trapped hydrogen does account for the degradation in the mechanical properties [58]. Furthermore, the susceptibility to HE becomes more serious as the basic strength is increased [59]. In order to conclude on the HE resistance of the developed X20CrNiMnVN18-5-10 MMnSS, a comparison with other previously investigated steels such as HMnS (X60Mn22, X60MnAl17-1 and X30MnAl22-1), MMnS (X5MnAl12-3) and a metastable stainless-steel 301 grade (X10CrNi17-7) is conducted and represented in Fig. 11. The percent of strain loss is considered as an indicator for the HE resistance. The main characteristics of the steels used for comparison are shown in Table 4 including the initial hydrogen content, which represents the metallurgical hydrogen measured after melt production. The comparison reveals that X20sCrNiMnVN18-5-10 steel with relatively high mechanical strength demonstrates an enhanced HE resistance. It exhibits a slightly better HE behavior to that of unsusceptible Al-modified HMnS but a superior one to that of other HMnS, MMnS and a metastable stainless steel. In Al-modified HMnS, the enhanced HE resistance was ascribed to postponing the formation of deformation twins (through increasing the SFE by Al-alloying), since deformation twin boundaries were found to act as favorable sites for crack initiation and enable crack propagation [21]. Additional feature that makes this X60MnAl17-1 steel resistant to HE is its fine microstructure (9 μm) that suppresses the early onset of deformation twinning and accommodates hydrogen at the large available grain boundary area [60], although the accumulation of hydrogen within the grain boundaries can lower the critical strain required to fracture [61]. The deformation induced α'-martensite controlled by the SFE is found to be detrimental to the HE resistance in metastable austenitic stainless steel at the similar strength level as the investigated steel [62]. Moreover, the large number of interfaces between α-γ/ α' phases in MMnS provides fast diffusing paths assisting in hydrogen damage [63], which could be improved by adjusting the state of the interfaces and the relative phase fractions [64].

In contrast, the X20CrNiMnVN18-5-10 MMnSS in this study possesses a significantly high density of hydrogen irreversible

Table 4 – Material characteristics that are relevant to hydrogen embrittlement behavior of the steel grades represented in Fig. 11.

Steel grade	Microstructure	Average GS [μm]	Tensile strength [MPa]	SFE [mJ/m^2]	Initial H content [ppm]
X20CrNiMnVN18-5-10	Austenitic	1.3	975	22.2	1.68
X60MnAl17-1 [60]	Austenitic	9	1011	25	1.6
X30MnAl22-1 [60]	Austenitic	19	633	24	5.9
X10CrNi17-7 [65,66]	Austenitic	24	923	11.2	1.1
X60Mn22 [60]	Austenitic	19	1087	30	1.7
X5MnAl12-3 [63]	55% Austenite	1.5	811	11-13	–

trapping sites within a stable austenitic microstructure with respect to hydrogen uptake, thus it demonstrates a superior intrinsic resistance to HE. The hydrogen irreversible trapping sites are owning to the nano-sized V- and Cr-based precipitates induced during short annealing. In addition to, the ultrafine recrystallized microstructure with an average grain size of 1.3 μm provides a large grain boundary area that limits the local hydrogen concentration, and subsequently hinders the premature fracture, despite the high hydrogen content that reaches 21.64 ppm. Moreover, the profound effect of grain refinement on suppressing deformation twins formation [43] maintains the microstructural stability and reduces the local inhomogeneities that can facilitate crack initiation. It is thus clear from the observed fracture mode near the surface of the pre-charged state that the progressive hydrogen uptake in the irreversible trapping sites, particularly those related to the large precipitates induced during production, promotes the hydrogen-enhanced localized plasticity (HELP) mechanism [67].

Hydrogen charging was found to cause phase transformation in the surface layer of charged specimens [68,69], such as martensitic transformation in austenitic steels, which is known as hydrogen-induced martensitic transformation [54]. This effect can explain the observed transition in fracture mode from fully ductile at the middle to trans-granular brittle near the surface of the pre-charged specimens (Fig. 8b and c). Furthermore, we pointed out in a previous report [43] that the local chemical changes in the vicinity of observed precipitates, in particular N and C contents, caused a decrease in SFE, which led to the formation of <1% ε-martensite and <2% α'-martensite at the fracture strain. Similar observation was reported in the Fe-15Cr-6Mn-3Ni-0.5Si-0.2N-0.1C containing VN precipitates, which caused in a grain boundary ductile fracture driven by strain-induced martensitic transformation due the local depletion of V and N in the vicinity of grain boundaries [70]. The formation of strain-induced α'-martensite, driven by either presence of precipitates or hydrogen precharging, of higher diffusivity than the austenite matrix [71] will provide fast transportation channels for hydrogen, which accounts for the increase in susceptibility to HE. However, in the deformed microstructure of this investigated steel, martensite is dilute decorated in the microstructure and does not lead to apparent degradation of the mechanical properties.

The investigated X20CrNiMnVN18-5-10 steel containing a significate amount of V- and Cr-based precipitates is originally developed considering a number of technological and material challenges related to processing as well as mechanical, corrosion and hydrogen embrittlement behaviors. It exhibits balanced mechanical and corrosion properties compared with other benchmark steels such as X60MnAl17-1 and X10CrNi18-8 [43]. The enhanced mechanical properties are achieved through the adjusted ultrafine grain microstructure with nano-precipitates, while the high corrosion resistance is owing to its designed chemistry with high Cr and N contents. The current study gives additionally an insight into utilizing this adjusted microstructure (ultrafine grains containing a high number density of nano-precipitates) as a HE-mitigation strategy, which can be applied to optimize the design of new HE-resistant advanced high strength MMnSS. Indeed, the observed different types of precipitates alleviate the HE by providing irreversible trapping sites, which makes the microstructure of X20CrNiMnVN18-5-10 steel insensitive to hydrogen uptake even at higher hydrogen levels than that can take place over service lifetime in some harsh application environment (~3 ppm). From the authors' point of view, there are still a number of open questions that remain for further studies regarding the fundamental physical understanding of hydrogen trapping by precipitates. For example, the determination of binding energies and quantification of number densities for different trapping sites, which allows a better prediction of HE susceptibility. Moreover, utilizing advanced high-resolution techniques with spatial elemental analysis capabilities e.g. atom probe tomography that can provide an insight into hydrogen distribution in different trapping sites. This will eventually lead to optimize the proposed HE-mitigation strategy by precipitates, and will open real opportunities in designing new HE-resistant steels.

5. Conclusions

In this study, the precipitation state was analyzed for an ultrafine grained (~1.3 μm) V-alloyed medium-manganese austenitic stainless steel X20CrNiMnVN18-5-10. The impact of precipitates on the hydrogen embrittlement behavior was investigated and discussed. Accordingly, the following conclusions can be drawn:

1 Three different size-groups of precipitates were identified, which correspond to different periods of precipitation. G-I (≥200 nm) comprises Fe-rich Cr(C) and Cr-rich V(N,C) particles, which formed during the casting and hot rolling processes. G-I I (~ 100 nm) and G-I II (~ 20 nm) consist of V/Cr(N) and Cr-rich V(N) particles, respectively, and they formed during the annealing heat treatment.
2 The observed precipitates with different sizes act as irreversible hydrogen trapping sites. The analysis of thermal

desorption spectroscopy (TDS) curves showed a size-dependent hydrogen desorption behavior and hydrogen uptake. The desorption peaks around and beyond 800 °C are attributed to the trapped hydrogen by large Cr(C) and V(N,C) precipitates. While, the desorption peaks at relatively lower temperatures (still >400 °C) correspond to the trapped hydrogen by the relatively large V/Cr(N) and small V(N) precipitates. The TDS analysis up to 800 °C for the pre-charged state indicated that the hydrogen uptake at the relatively large V/Cr(N) precipitates is larger than that occurs at the small V(N) precipitates.

3 The pre-charged state with a significant amount of diffusive hydrogen (11.50 ppm) exhibits a mild degradation in strength and ductility values compared with the annealed state without pre-charging. Yield strength, ultimate tensile strength and uniform elongation decrease from 616 MPa, 944 MPa and 38.6 % to 553 MPa, 868 MPa and 25.7 %, respectively.

4 The investigated X20CrNiMnVN18-5-10 steel in the annealed state exhibits a low sensitivity to hydrogen uptake during charging and demonstrates an enhanced intrinsic resistance to hydrogen embrittlement (HE) compared with X60MnAl17-1, X30MnAl22-1, X10CrNi17-7, X60Mn22 and X5MnAl12-3 steels. This enhanced resistance to HE is owing to the ultrafine-grained microstructure that contains a significant amount of precipitates, which provide a high density of irreversible trapping sites.

The current work gives an insight into improving the intrinsic resistance of steels against hydrogen embrittlement by adjusting an ultrafine-grained microstructure containing a significant amount of precipitates that acts as irreversible hydrogen trapping sites, given that the mechanical properties will not be deteriorated and satisfy the application requirements.

Declaration of interests

The authors declare that they have no known competing financial interests or personal relationships that could have appeared to influence the work reported in this paper.

Acknowledgement

The German research foundation (DFG) within the Collaborative Research Center SFB 761 is appreciated for supporting the processing and testing the developed steel grade. TA acknowledges the DAAD for the personal financial support during the testing phase. The material of this work was produced within the project of National Challenges Program (STDF-NCP-10751) funded by the Science and Technology Development Fund (STDF), The Egyptian Ministry of Higher Education and Scientific Research, Cairo.

REFERENCES

[1] Bouaziz O, Allain S, Scott CP, Cugy P, Barbier D. High manganese austenitic twinning induced plasticity steels: a review of the microstructure properties relationships. Curr Opin Solid State Mater Sci 2011;15(4):141–68, http://dx.doi.org/10.1016/j.cossms.2011.04.002.

[2] Chiaberge Marcello, editor. New trends and developments in automotive system engineering. High Mn TWIP steels for automotive applications. IntechOpen; 2011.

[3] Chin K-G, Kang C-Y, Shin SY, Hong S, Lee S, Kim HS, et al. Effects of Al addition on deformation and fracture mechanisms in two high manganese TWIP steels. Mater Sci Eng A 2011;528(6):2922–8, http://dx.doi.org/10.1016/j.msea.2010.12.085.

[4] Koyama M, Akiyama E, Tsuzaki K. Effect of hydrogen content on the embrittlement in a Fe–Mn–C twinning-induced plasticity steel. Corros Sci 2012;59:277–81, http://dx.doi.org/10.1016/j.corsci.2012.03.009.

[5] Chun YS, Park K-T, Lee CS. Delayed static failure of twinning-induced plasticity steels. Scr Mater 2012;66(12):960–5, http://dx.doi.org/10.1016/j.scriptamat.2012.02.038.

[6] Grajcar A. Corrosion resistance of high-Mn austenitic steels for the automotive industry. In: Shih H, editor. Corrosion resistance. Rijeka: InTech; 2012.

[7] Zhang YS, Zhu XM. Electrochemical polarization and passive film analysis of austenitic Fe-Mn-Al steels in aqueous solutions. Corros Sci 1999;41:1817–33.

[8] Zhang YS, Zhu XM, Liu M, Che RX. Effects of anodic passivation on the constitution, stability and resistance to corrosion of passive film formed on an Fe-24Mn-4Al-5Cr alloy. Appl Surf Sci 2004;222(1–4):89–101, http://dx.doi.org/10.1016/j.apsusc.2003.08.068.

[9] Hamada AS, Karjalainen LP, El-Zeky MA, editors. Effect of anodic passivation on the corrosion behaviour of Fe-Mn-Al steels in 3.5%NaCl: passivation of metals and semiconductors, and properties of thin oxide layers. Elsevier; 2006.

[10] Kannan MB, Raman RS, Khoddam S. Comparative studies on the corrosion properties of a Fe–Mn–Al–Si steel and an interstitial-free steel. Corros Sci 2008;50(10):2879–84, http://dx.doi.org/10.1016/j.corsci.2008.07.024.

[11] Okada T, Hashino T. A contribution to the kinetic theory of Pitting Corrosion. Corros Sci 1977;17:671–89.

[12] Gavriljuk VG, Berns H. High nitrogen steels: structure, properties, manufacture, applications. Berlin Heidelberg: Springer-Verlag; 1999.

[13] Stoltz RE, Vander Saude JB. The effect of nitrogen on stacking fault energy of Fe-Ni-Cr-Mn steels. Metall Mat Trans A 1980;11A:1033–7.

[14] Toor I-u-H, Hyun PJ, Kwon HS. Development of high Mn–N duplex stainless steel for automobile structural components. Corros Sci 2008;50(2):404–10, http://dx.doi.org/10.1016/j.corsci.2007.07.004.

[15] Mosecker L, Saeed-Akbari A. Nitrogen in chromium-manganese stainless steels: a review on the evaluation of stacking fault energy by computational thermodynamics. Sci Technol Adv Mater 2013;14(3):33001, http://dx.doi.org/10.1088/1468-6996/14/3/033001.

[16] Mosecker L, Pierce DT, Schwedt A, Beighmohamadi M, Mayer J, Bleck W, et al. Temperature effect on deformation mechanisms and mechanical properties of a high manganese C+N alloyed austenitic stainless steel. Mater Sci Eng A 2015;642:71–83, http://dx.doi.org/10.1016/j.msea.2015.06.047.

[17] Lee T-H, Oh C-S, Kim S-J. Effects of nitrogen on deformation-induced martensitic transformation in metastable austenitic Fe–18Cr–10Mn–N steels. Scr Mater 2008;58(2):110–3, http://dx.doi.org/10.1016/j.scriptamat.2007.09.029.

[18] Berns H, Nabiran N, Mujica L. High-interstitial stainless austenitic steel castings. Steel Res Int 2013;84(2):119–28, http://dx.doi.org/10.1002/srin.201100332.
[19] Dieudonné T, Marchetti L, Wery M, Chêne J, Allely C, Cugy P, et al. Role of copper and aluminum additions on the hydrogen embrittlement susceptibility of austenitic Fe–Mn–C TWIP steels. Corros Sci 2014;82:218–26, http://dx.doi.org/10.1016/j.corsci.2014.01.022.
[20] Ryu JH, Kim SK, Lee CS, Suh D-W, Bhadeshia HKDH. Effect of aluminium on hydrogen-induced fracture behaviour in austenitic Fe-Mn-C steel. Proc R Soc A: Math Phys Eng Sci 2012;469(2149):20120458, http://dx.doi.org/10.1098/rspa.2012.0458.
[21] Koyama M, Akiyama E, Lee Y-K, Raabe D, Tsuzaki K. Overview of hydrogen embrittlement in high-Mn steels. Int J Hydrogen Energy 2017;42(17):12706–23, http://dx.doi.org/10.1016/j.ijhydene.2017.02.214.
[22] Hong S, Lee J, Lee B-J, Kim HS, Kim S-K, Chin K-G, et al. Effects of intergranular carbide precipitation on delayed fracture behavior in three twinning induced plasticity (TWIP) steels. Mater Sci Eng A 2013;587:85–99, http://dx.doi.org/10.1016/j.msea.2013.08.063.
[23] Dumay A, Chateau J-P, Allain S, Migot S, Bouaziz O. Influence of addition elements on the stacking-fault energy and mechanical properties of an austenitic Fe–Mn–C steel. Mater Sci Eng A 2008;483–484:184–7, http://dx.doi.org/10.1016/j.msea.2006.12.170.
[24] Kim Y, Kang N, Park Y, Choi I, Kim G, Kim S, et al. Effects of the strain induced martensite transformation on the delayed fracture for Al-added TWIP steel. J Korean Inst Metals Mater 2008;46:780–7.
[25] Koyama M, Akiyama E, Tsuzaki K. Hydrogen embrittlement in Al-added twinning-induced plasticity steels evaluated by tensile tests during hydrogen charging. ISIJ Int 2012;52(12):2283–7.
[26] Zan N, Ding H, Guo X, Tang Z, Bleck W. Effects of grain size on hydrogen embrittlement in a Fe-22Mn-0.6C TWIP steel. Int J Hydrogen Energy 2015;40(33):10687–96, http://dx.doi.org/10.1016/j.ijhydene.2015.06.112.
[27] Bai Y, Momotani Y, Chen MC, Shibata A, Tsuji N. Effect of grain refinement on hydrogen embrittlement behaviors of high-Mn TWIP steel. Mater Sci Eng A 2016;651:935–44, http://dx.doi.org/10.1016/j.msea.2015.11.017.
[28] Ooi SW, Ramjaun TI, Hulme-Smith C, Morana R, Drakopoulos M, Bhadeshia HKDH. Designing steel to resist hydrogen embrittlement Part 2 – precipitate characterisation. Mater Sci Technol 2018;34(14):1747–58, http://dx.doi.org/10.1080/02670836.2018.1496536.
[29] Zhang Z, Moore KL, McMahon G, Morana R, Preuss M. On the role of precipitates in hydrogen trapping and hydrogen embrittlement of a nickel-based superalloy. Corros Sci 2019;146:58–69, http://dx.doi.org/10.1016/j.corsci.2018.10.019.
[30] Takahashi J, Kawakami K, Kobayashi Y. Origin of hydrogen trapping site in vanadium carbide precipitation strengthening steel. Acta Mater 2018;153:193–204, http://dx.doi.org/10.1016/j.actamat.2018.05.003.
[31] Timmerscheidt T, Dey P, Bogdanovski D, von Appen J, Hickel T, Neugebauer J, et al. The role of κ-Carbides as hydrogen traps in High-Mn steels. Metals 2017;7(7):264, http://dx.doi.org/10.3390/met7070264.
[32] Malard B, Remy B, Scott C, Deschamps A, Chêne J, Dieudonné T, et al. Hydrogen trapping by VC precipitates and structural defects in a high strength Fe–Mn–C steel studied by small-angle neutron scattering. Mater Sci Eng A 2012;536:110–6, http://dx.doi.org/10.1016/j.msea.2011.12.080.
[33] Nagao A, Martin ML, Dadfarnia M, Sofronis P, Robertson IM. The effect of nanosized (Ti,Mo)C precipitates on hydrogen embrittlement of tempered lath martensitic steel. Acta Mater 2014;74:244–54, http://dx.doi.org/10.1016/j.actamat.2014.04.051.
[34] Depover T, Monbaliu O, Wallaert E, Verbeken K. Effect of Ti, Mo and Cr based precipitates on the hydrogen trapping and embrittlement of Fe–C–X Q&T alloys. Int J Hydrogen Energy 2015;40(47):16977–84, http://dx.doi.org/10.1016/j.ijhydene.2015.06.157.
[35] Wei F-G, Hara T, Tsuzaki K. Nano-percipitates design with hydrogen trapping character in high strength steel. In: Proceedings of the 2008 International Hydrogen Conference - Effects of Hydrogen on Materials. 2009. p. 448–55.
[36] Turk A, San Martín D, Rivera-Díaz-del-Castillo PEJ, Galindo-Nava EI. Correlation between vanadium carbide size and hydrogen trapping in ferritic steel. Scr Mater 2018;152:112–6, http://dx.doi.org/10.1016/j.scriptamat.2018.04.013.
[37] Cooman de BC. High Mn TWIP steel and medium Mn steel. In: Automotive steels. Elsevier; 2017. p. 317–85.
[38] Rana R, de Moor E, Speer JG, Matlock DK. Effects of hot band annealing on the mechanical properties of cold-rolled and intercritically annealed medium manganese steels. Metall and Mat Trans A 2019;50(9):4016–20, http://dx.doi.org/10.1007/s11661-019-05363-1.
[39] Lee Y-K, Han J. Current opinion in medium manganese steel. Mater Sci Technol 2015;31(7):843–56, http://dx.doi.org/10.1179/1743284714Y.0000000722.
[40] da Silva AK, Inden G, Kumar A, Ponge D, Gault B, Raabe D. Competition between formation of carbides and reversed austenite during tempering of a medium-manganese steel studied by thermodynamic-kinetic simulations and atom probe tomography. Acta Mater 2018;147:165–75.
[41] Hamada A, Kömi J. Effect of microstructure on mechanical properties of a novel high-Mn TWIP stainless steel bearing vanadium. Mater Sci Eng A 2018;718:301–4, http://dx.doi.org/10.1016/j.msea.2018.01.132.
[42] Hamada A, Juuti T, Khosravifard A, Kisko A, Karjalainen P, Porter D, et al. Effect of silicon on the hot deformation behavior of microalloyed TWIP-type stainless steels. Mater Des 2018;154:117–29, http://dx.doi.org/10.1016/j.matdes.2018.05.029.
[43] Allam T, Guo X, Sevsek S, Lipińska-Chwałek M, Hamada A, Ahmed E, et al. Development of a Cr-Ni-V-N medium manganese steel with balanced mechanical and corrosion properties. Metals 2019;9(6):705, http://dx.doi.org/10.3390/met9060705.
[44] Luysberg M, Heggen M, Tillmann K. FEI tecnai G2 F20. JLSRF 2016:2, http://dx.doi.org/10.17815/jlsrf-2-138.
[45] Kovács A, Schierholz R, Tillmann K. FEI titan G2 80-200 CREWLEY. JLSRF 2016:2, http://dx.doi.org/10.17815/jlsrf-2-68.
[46] Li D, Gangloff RP, Scully JR. Hydrogen trap states in ultrahigh-strength AERMET 100 steel. Metall and Mat Trans A 2004;35(3):849–64, http://dx.doi.org/10.1007/s11661-004-0011-1.
[47] Frappart S, Oudriss A, Feaugas X, Creus J, Bouhattate J, Thébault F, et al. Hydrogen trapping in martensitic steel investigated using electrochemical permeation and thermal desorption spectroscopy. Scr Mater 2011;65(10):859–62, http://dx.doi.org/10.1016/j.scriptamat.2011.07.042.
[48] Lee SM, Lee JY. The effect of the interface character of TiC particles on hydrogen trapping in steel. Acta Metall 1987;35(11):2695–700, http://dx.doi.org/10.1016/0001-6160(87)90268-9.
[49] Koyama M, Springer H, Merzlikin SV, Tsuzaki K, Akiyama E, Raabe D. Hydrogen embrittlement associated with strain localization in a precipitation-hardened Fe–Mn–Al–C light weight austenitic steel. Int J Hydrogen Energy 2014;39(9):4634–46, http://dx.doi.org/10.1016/j.ijhydene.2013.12.171.

[50] Choo WY, Lee JY. Thermal analysis of trapped hydrogen in pure iron. MTA 1982;13(1):135–40, http://dx.doi.org/10.1007/BF02642424.
[51] Scott C., Cugy P. Vanadium additions in new ultra high strength and ductility steels. In proceeding of 2009 International Symposium on Automobile Steel (ISAS'09), Dalian, China, 6-8 September 2009.
[52] Pressouyre GM, Bernstein IM. A kinetic trapping model for hydrogen-induced cracking. Acta Metall 1979;27(1):89–100, http://dx.doi.org/10.1016/0001-6160(79)90059-2.
[53] Pressouyre GM, Bernstein IM. A quantitative analysis of hydrogen trapping. MTA 1978;9(11):1571–80, http://dx.doi.org/10.1007/BF02661939.
[54] Barrera O, Bombac D, Chen Y, Daff TD, Galindo-Nava E, Gong P, et al. Understanding and mitigating hydrogen embrittlement of steels: a review of experimental, modelling and design progress from atomistic to continuum. J Mater Sci 2018;53(14):10593–4, http://dx.doi.org/10.1007/s10853-018-2291-7.
[55] Di Stefano D, Nazarov R, Hickel T, Neugebauer J, Mrovec M, Elsässer C. First-principles investigation of hydrogen interaction with TiC precipitates in α -Fe. Phys Rev B 2016;93(18):22, http://dx.doi.org/10.1103/PhysRevB.93.184108.
[56] Hallberg M, Jonsson TLI, Jönsson PG. A new approach to using modelling for on-line prediction of sulphur and hydrogen removal during ladle refining. ISIJ Int 2004;44(8):1318–27, http://dx.doi.org/10.2355/isijinternational.44.1318.
[57] Gao Q, Han F, Wortberg D, Bleck W, Liewald M. Influence of hydrogen on formability and bendability of DP1180 steel for car body application. IOP Conf Ser Mater Sci Eng 2016;159:12010, http://dx.doi.org/10.1088/1757-899X/159/1/012010.
[58] Bhadeshia HKDH. Prevention of hydrogen embrittlement in steels. ISIJ Int 2016;56(1):24–36, http://dx.doi.org/10.2355/isijinternational.ISIJINT-2015-430.
[59] Johnson HH. Hydrogen embrittlement. Science 1973;179(4070):228–30, http://dx.doi.org/10.1126/science.179.4070.228-c.
[60] Guo X, Schwedt A, Richter S, Bleck W. Effects of Al on delayed fracture in TWIP steels discussion from the aspects of structure homogeneity, hydrogen traps, and corrosion resistance. In: 2nd International Conference on Metals and Hydrogen. 2014.
[61] Du YA, Ismer L, Rogal J, Hickel T, Neugebauer J, Drautz R. First-principles study on the interaction of H interstitials with grain boundaries in α - and γ -Fe. Phys Rev B 2011;84(14):456, http://dx.doi.org/10.1103/PhysRevB.84.144121.
[62] Lo KH, Shek CH, Lai JKL. Recent developments in stainless steels. Mater Sci Eng R Rep 2009;65(4-6):39–104, http://dx.doi.org/10.1016/j.mser.2009.03.001.
[63] Shen X, Song W, Sevsek S, Ma Y, Hüter C, Spatschek R, et al. Influence of microstructural morphology on hydrogen embrittlement in a Medium-Mn steel Fe-12Mn-3Al-0.05C. Metals 2019;9(9):929, http://dx.doi.org/10.3390/met9090929.
[64] Sun B, Krieger W, Rohwerder M, Ponge D, Raabe D. Dependence of hydrogen embrittlement mechanisms on microstructure-driven hydrogen distribution in medium Mn steels. Acta Mater 2020;183:313–28, http://dx.doi.org/10.1016/j.actamat.2019.11.029.
[65] Guo X, Post J, Groen M, Bleck W. Stress oriented delayed cracking induced by dynamic martensitic transformation in meta-stable austenitic stainless steels. Steel Res Int 2011;82(1):6–13, http://dx.doi.org/10.1002/srin.201000234.
[66] Guo X, Bleck W. Influences of material and process parameters on delayed fracture in TRIP-aided austenitic stainless steels. In: Supplemental proceedings. Hoboken, NJ, USA: John Wiley & Sons, Inc; 2011. p. 521–8.
[67] Birnbaum HK, Sofronis P. Hydrogen-enhanced localized plasticity—a mechanism for hydrogen-related fracture. Mater Sci Eng A 1994;176(1–2):191–202, http://dx.doi.org/10.1016/0921-5093(94)90975-X.
[68] Hoelzel M, Danilkin SA, Ehrenberg H, Toebbens DM, Udovic TJ, Fuess H, et al. Effects of high-pressure hydrogen charging on the structure of austenitic stainless steels. Mater Sci Eng A 2004;384(1-2):255–61, http://dx.doi.org/10.1016/j.msea.2004.06.017.
[69] Nishino Y, Obata M, Asano S. Hydrogen-induced phase transformations in Fe50Ni50−xMnx alloys. Scr Metall Mater 1990;24(4):703–8, http://dx.doi.org/10.1016/0956-716X(90)90227-8.
[70] Wendler M, Reichel B, Eckner R, Fabrichnaya O, Krüger L, Weiß A, et al. Effect of vanadium nitride precipitation on martensitic transformation and mechanical properties of CrMnNi cast austenitic steels. Metall and Mat Trans A 2016;47(1):139–51, http://dx.doi.org/10.1007/s11661-.
[71] Sanmarchi C. Effects of alloy composition and strain hardening on tensile fracture of hydrogen-precharged type 316 stainless steels. Int J Hydrogen Energy 2008;33(2):889–904, http://dx.doi.org/10.1016/j.ijhydene.2007.10.046.